Journal of Materials Chemistry A

Accepted Manuscript

ROYAL SOCIETY OF CHEMISTRY

www.rsc.org/materialsA

Journal Name

ARTICLE

Catalytic Effect of Two-Phase Intergrowth and Coexistence CuO-CeO_2

Jiahui Ma,[a] Guangzhou Jin,[a]* Junbin Gao,[a] Yuyang Li,[a] Lihui Dong,[b]* Meina Huang,[b] Qingqing Huang[b] and Bin Li[b]

Received 00th January 20xx,
Accepted 00th January 20xx

DOI: 10.1039/x0xx00000x

www.rsc.org/

The intergrowth CuO-CeO_2 oxides were synthesized by an improved amorphous citric precursor (IACP) method. In order to explore the relationship between structure modulation and catalytic performance, samples were characterized by XRD, XPS, SEM, EDX, HRTEM, O_2-TPD, TG-DSC, OSC, H_2-TPR, and *in situ* DRIFTS measurements. Catalytic activities were then investigated in CO+O_2 and NO+CO model reactions. Results indicate that CuO-CeO_2 samples form an intergrowth system which is made up of imperfect monoclinic crystal CuO and cubic crystal CeO_2. Strong interactions between CuO and CeO_2 occurred in intergrowth process, making Cu species of CuO gradually form Cu^+ and produce corresponding oxygen vacancy with the increase of CeO_2 content, which results in imperfect $[Cu^{2+}_{1-x}Cu^{+}_{x}][O_{1-x/2}\square_{x/2}]$ structure and improvement of redox ability of CuO. Meanwhile, CeO_2 remains a few Ce^{3+} and corresponding oxygen vacancy. As a result, the OSC and catalytic performance of samples are greatly enhanced. These results are partly due to the intergrowth and coexistence effects of CuO-CeO_2.

Introduction

With the increasing environmental protection awareness and the enforcement of worldwide regulations, atmosphere contamination treatment attracts much attention of the researchers.[1] CO and NO as the main atmosphere pollutants are emitted from stationary sources (e.g., coal-fired power plants) and mobile sources (e.g., vehicle exhausts), moreover, with the rapid development of automobile industry, the vehicle tail gas pollution causes serious threat to human health. On the one hand, NO cannot only cause the photochemical smog and acid rain, but also induce the ozone depletion and greenhouse effect; on the other hand, CO can easily unite with the hemoglobin in the human body but separate difficultly. In addition, CO oxidation is a fundamental step in some important industrial processes such as production of methanol and water gas shift reaction.[2,3]

As potential catalyst, CuO/CeO_2 system has been demonstrated high activity towards 1,2-dichlorobenzene oxidation, the CO+O_2 and CO+NO reactions.[4-19] Martínez-Arias et al[8] has prepared and studied the CuO/CeO_2 catalyst and found that there is a novel promoting effect of NO on CO oxidation resulting from the phenomena of adsorption/desorption of NO_x species at interfacial positions, which apparently activate such interfacial region, allowing formation of greater amounts of reduced copper active site in the presence of NO. Lu et al[9] gave a full and accurate characterization of copper oxide catalysts supported on various types of CeO_2 supports and reported that CuO supported on CeO_2 that was self-prepared by pyrolysis had a large pore volume and good crystal structure of CeO_2, showing high activity for CO oxidation at low temperature.

The influence of coexistence effects on the microstructure and the catalytic activity has become a primary focus of researchers in recent years.[20,21] In addition, nanocomposite materials possess distinct properties arising from the interaction of their phases at the interface.[22] Schwab and Pietsch et al[23-26] reported that existence of ''adlineation'' or active sites located at the interface of two solid phases. They postulated that enhanced chemical activity existed at the interfaces of crystals in polycrystalline materials.[26] However, most of the CuO/CeO_2 catalysts are supported catalysts which CeO_2 acts as support and CuO acts as active component dispersing on CeO_2 surface. There is no investigation of the intergrowth and coexistence effects of the mixed phase CuO-CeO_2 catalyst in open literature. Based on the discussion above, it is necessary to prepare two phase intergrowth and coexistence CuO-CeO_2 catalyst in this study. Moreover, it is important to understand the mechanism of CuO-CeO_2 with two-phase intergrowth and coexistence catalytic effects for designing and developing highly active catalysts. In our previous works, we have studied biphasic intergrowth effects in TiO_2-SnO_2 nanocomposite,[27] CeO_2-γ-Al_2O_3 mixed oxides[28] and CuO-γ-Al_2O_3 mixed oxides[29] prepared by IACP method.[30,31] The effects of the preparation method on the structure and properties were discussed.[32]

Herein, in the present study, a series of CuO-CeO_2 catalysts with different molar ratios were prepared through IACP method. This study was mainly focused on: (i) Exploring the forming mechanism of two-phase intergrowth and coexistence CuO-CeO_2 catalyst and its effect on structure reset; (ii) Exploring the catalytic effect of CuO-CeO_2 for CO+O_2 and NO+CO model reactions.

[a] Department of Chemical Engineering, Beijing Institute of Petro-Chemical Technology, Beijing 102617, China.
[b] Guangxi Key Laboratory Petrochemical Rescource Processing and Process Intensification Technology, School of Chemistry and Chemical Engineering, Guangxi University, Nanning 530004, China.

Experimental

2.1. Sample preparation

Pure CuO and CeO_2 as well as CuO-CeO_2 composite were prepared by the IACP method. The method was modified compared to the reported previously.[33] In brief, an aqueous salt solution containing 1.752 mol/L $Cu(NO_3)_2$•$3H_2O$ (AR, Beijing Chemical Reagent Plant, China), 3 M $Ce(NO_3)_3$•$6H_2O$ (AR, Beijing Chemical Reagent Plant, China) was prepared, respectively. Then they were mixed according to different molar ratios (Cu:Ce = 10:0, 9:1, 8:2, 7:3, 6:4, 5:5, 4:6, 3:7, 2:8, 1:9, 0:10). Appropriate citric acid (AR) was then added to this solution. The solution and citric acid were mixed by sufficient agitation. After 12 h, the solution was added dropwise onto appropriate carbon black. The wet carbon black was dried at 100 °C, ground into a fine powder, decomposed at 230 °C for 2 h, and calcined at 700 °C under air flow for 3 h, then a series of black powers were obtained. For simplification, the samples were denoted as Cu_mCe_n, for example, the molar ratio Cu:Ce = 9:1 was denoted as Cu_9Ce_1. For comparison purposes, a series of mechanical mixture samples with the same molar ratio of Cu_mCe_n were prepared by mixing pure CuO and CeO_2, which was denoted as Cu_mCe_n-M.

2.2. Characterization methods

Powder X-ray diffraction (XRD) measurements were conducted at room temperature (RT) with a Rigaku D/max2000 diffractometer by employing Cu K_α radiation (λ=1.5406 Å); the instrument was operated at a voltage of 40 kV, current of 100 mA, entrance slit for 1° and receiving slit for 3 mm. Step scans were obtained over the 2θ range of 30-80° with a step size of 1°/min. The intensities of each point were determined for 2 s for phase identification and lattice parameter calculation. Scanning electron microscopy (SEM) and energy-dispersive X-ray spectrometry (EDX) were performed using HITACHI-3500N at a voltage of 20 kV. Transmission electron microscopy (TEM) was employed a JEOL JEM-2000EX and a FEI Tecnai G^2 Spirit at an acceleration voltage of 120 kV. HRTEM images were obtained on Tecnai G^2 F30 S-Twin (FEI Company). Thermogravimetric and Differential Scanning Calorimetry (TG/DSC) were carried out on a Netsch 40PC TG/DSC simultaneous thermal analyzer. The sample was placed in alumina crucible under 40 mL/min air atmosphere at a heating of 10 °C/min.

X-ray photoelectron spectroscopy (XPS) was performed on an AXIS-Ultra of Kratos Analytical Company in Britain, using monochromatic Al Kα radiation (15 mA, 15 kV). Electron binding energy is based on C 1*s* (284.6 eV), sample irradiation area and detecting depth are 2 mm*1 mm and 2-5 nm, respectively. The reducibility of the samples was examined by H_2 temperature programmed reduction (H_2-TPR) through a FINESORB-3010 Chemisorption Analyzer. About 50 mg of sample (40-60 mesh) was employed for each test. The sample was pretreated in N_2 stream at 400 °C for 40 min and then cooled to room temperature. After that, a 15% H_2/Ar mixture (15% H_2 by volume) was switched on for 30 min and then the temperature increased from RT to 700 °C (10 °C/min), H_2 consumption was analyzed by using thermal conductivity detector. O_2-TPD was carried out on an automated chemisoption analyzer (Finetec Instruments). First, 100 mg of the sample was heated in He (50 mL/min) from room temperature to 200 °C and held for 1 h, subsequently cooled to room temperature in a He atmosphere and switched to pure O_2 (10 mL/min)) and held for 0.5 h. After that, it was purged by He for 0.5 h for removal of residual gas. Then the sample was heated from room temperature to 700 °C in He at a heating rate of 10 °C/min. The consumption of O_2 was continuously monitored using a thermal conductivity detector.

In situ diffuse reflectance infrared Fourier transform spectra (*in situ* DRIFTS) were collected from 650 to 4000 cm^{-1} at a spectral resolution of 4 cm^{-1} (number of scans, 32) on a Nicolet 5700 FT-IR spectrometer equipped with a high-sensitive MCT detector cooled by liquid N_2. The DRIFTS cell (Harrick) was fitted with a ZnSe window and a heating cartridge that allowed sample to be heated to 400 °C. The fine catalyst powder placed on a sample holder was carefully flattened to enhance IR reflection. The sample was pretreated with a high purified N_2 stream at 300 °C for 1 h to eliminate the physisorbed water and other impurities. The sample background of each target temperature was collected during the cooling process. At ambient temperature, the sample was exposed to a controlled stream of CO-Ar (10% of CO by volume) or NO-Ar (5% of NO by volume) at a rate of 5.0 mL/min for 1 h to be saturated. Desorption/reaction studies were performed by heating the adsorbed species and the spectra were recorded at various target temperatures at a rate of 10 °C/min from room temperature to 250 °C by subtraction of the corresponding background reference.

2.3. Performance evaluation

2.3.1. OSC determination

According to the traditional oxygen storage capacity (OSC) measurement,[34] OSC measurements were carried out in Multi-purpose adsorption instrument (Tianjin Xianquan Instrument Co., Ltd., China). And the results were processed by data processing system of Multi-purpose adsorption instrument.

2.3.2. Activity measurement for CO oxidation

The activities of the catalysts in CO+O_2 reaction were measured in a continuous micro-reactor with a gas composition of CO 6.0% (V), O_2 3.6% (V) and He in balance with a space velocity of 20 sL/g·h. The powder samples were pressed into tablets under 20 MPa, crushed into small pieces, and sieved. 20±0.1 mg sample (40-60 mesh) was fully mixed with 2.0 g quartz sand as diluents (40-60 mesh pretreated 24 h in aqua regia and dried at 100 °C after washing with deionized water). The mixture was charged into a quartz tube reactor and fixed by two pieces of silica wool. Catalysts were pretreated in a N_2 stream at 100 °C for 1 h before being switched to the reaction gas stream. The temperature of reaction bed was controlled with armored thermocouple (±0.1 K). Tail gases were measured with a gas chromatograph (GC-7890T, Shanghai scientific instrument co., LTD) equipped with a thermal conductivity detector. Reactions were carried out at different temperatures. CO conversion was calculated after 1 h at each temperature. Each data point was obtained from the average of 5 test results. The CO conversion values were calculated as follows:

$$\text{CO conversion (\%)} = [(CO)_{in}\text{-}(CO)_{out}]*100 \quad \text{(Eq. A.1)}$$

In addition, T_{50} and T_{90} signify the temperatures at which the CO conversion reaches 50% and 90%, respectively.

2.3.3. Activity measurement for NO reduction

The catalytic performances of these samples for NO reduction by CO were determined under sequential and steady state, involving a feed stream with a fixed composition, 5% NO, 10% CO, and 85% He

by volume as a diluent. 50 mg (40-60 mesh) were fitted in a quartz tube and pretreated in a highly purified N_2 stream at 110 °C for 1 h to remove the impurities and then cooled to ambient temperature before the mixed gases were switched on. The reactions were carried out at different temperatures from 150-300 °C with a space velocity of 24 sL/g·h. Active data was collected after the reaction equilibrium.

Results and discussion

3.1. XRD results

The X-ray diffraction patterns of the samples with different molar ratios of Cu to Ce are shown in Fig. 1. Pure CuO and CeO_2 are also prepared for comparison. For the Cu_1Ce_9, Cu_2Ce_8, and Cu_3Ce_7, the relative content of CuO is far less and its diffractivity is weaker than CeO_2, consequently, the diffraction patterns (Fig. 2) were obtained over the 2θ range of 60-85° which the CeO_2 diffraction peaks are fewer and weaker, moreover, the incident intensity of X-ray is reinforced so that the diffraction peak of CuO phase can be obserbed..

It can be seen that all diffraction peaks in Fig. 1 and Fig. 2 can be easily indexed to CeO_2 and CuO JCPDS card (34-0394 and 48-1548), no impurity peaks are found, indicating high purity of the samples. Therefore, it can be indicated that the as-prepared CuO-CeO_2 samples form an intergrowth and coexistence system which is made up of imperfect monoclinic crystal CuO and cubic crystal CeO_2. According to least-squares refinement of the d-spacings measured from the XRD trace,[35] the lattice parameter of these samples is summarized in Table 1. It shows that for the two-phase intergrowth and coexistence CuO-CeO_2 samples, the lattice parameter of CuO phase increases with increasing CeO_2 content, however, the lattice parameter of CeO_2 phase has relatively little change. The varying cell volumes curve of the Cu_mCe_n samples is shown in Fig. 3. It shows the variation law of the lattice parameter of CuO-CeO_2 samples. The findings suggest that CeO_2 content has great effect on CuO network, however, the structure of CeO_2 has nothing to do with CuO content.

3.2. SEM and EDX results

The morphology and uniformity of the intergrowth samples can be further confirmed by SEM and EDX characterization of Cu_6Ce_4 and corresponding mechanically mixed Cu_6Ce_4-M samples (Fig. 4). It shows that the Cu_6Ce_4 composes of uniform, well-distributed particles and no cracks and abnormal large particles are observed (Fig. 4A1), whereas the Cu_6Ce_4-M sample (Fig. 4B1) composes of a large number of non-uniforms. Most of them are strongly agglomerated particles, at the same time, there are a few small particles. In order to prove the intergrowth effect, EDX mapping images of the relevant samples are shown in Fig. 4A2 (Cu_6Ce_4) and B2 (Cu_6Ce_4-M), the red areas represent Ce enrichment region and the green areas represent Cu enrichment region. The Cu_6Ce_4 shows no obvious Ce and Cu enrichment region (Fig. 4A2). However, the Cu_6Ce_4-M shows serious Ce and Cu enrichment region. Furthermore, Fig. 4A3-A4 (Cu_6Ce_4) and Fig. 4B3-B4 (Cu_6Ce_4-M) show the elemental distributions. It can be seen that the light and shade degree of the Cu_6Ce_4 (Fig. 4A3-A4) is far more uniform than the Cu_6Ce_4-M (Fig. 4B3-B4), revealing that the elemental distribution of mechanically mixed sample is far from well distributed. These results suggest that CuO-CeO_2 is intergrowth composite oxide which has a strong interaction between CuO and CeO_2 phase resulting in the elements well-distributed, in good agreement with the XRD results.

3.3. Transmission electron microscopy (TEM)

TEM measurements were performed in order to complement the structural analyses of the CuO-CeO_2. Fig. 5 illustrates the images of the representative catalyst (Cu_5Ce_5) examined by TEM and HRTEM. TEM shows that the diameters of most particles are in a range between 10 and 50 nm with particles contacting each other intimately (Fig. 5a). HRTEM studies further provide crucial information on the spatial distribution. Fig. 5b displays the atomic planes with a lattice spacing of 0.304 nm and 0.159 nm, which can be indexed into (111) atomic plane of CeO_2 and (202) atomic plane of CuO, respectively. Further proving that the Cu_5Ce_5 sample is consisted of intergrowth two phase. However, the lattice spacing of CeO_2 is smaller than the JCPDS card (34-0394) and reported reference,[10] but for the CuO, it is a little larger than JCPDS card (48-1548), which may be attributed to the strong mutual interactions between two phases resulting in the lattice distortions. These results are proved directly by the interface between CuO and CeO_2, as shown in Fig. 5b, the interface zone crystal structure is disrupted obviously. This result may due to the strong mutual interactions resulting in the disruption of the interface zone.[36]

HRTEM displays the combination of surface monoclinic crystal CuO in intimate contact with cubic crystal CeO_2. Furthermore, HRTEM images together with TEM images provided direct evidence for the phase junction between monoclinic crystal CuO and cubic crystal CeO_2.

3.4. Chemical states analysis (XPS)

The catalyst systems are analyzed by XPS to verify surface composition and elementary oxidation states. Fig. 6 shows the XPS spectra of Cu 2p, Cu LMMa, Ce 3d and O 1s for Cu_mCe_n samples. The Cu $2p_{3/2}$ characteristic peak of pure CuO sample is observed at 934.1 eV (Fig. 6a). Moreover, it can be seen that there are obvious satellite peaks between 940.6-943.4 eV which is the signal of Cu^{2+} characteristic peak.[37] For the intergrowth CuO-CeO_2 samples, the satellite peaks wear off and the characteristic peak at 933.6 eV (Cu $2p_{3/2}$) shifts to lower binding energy values than that of CuO with the increase of CeO_2 content (Table 2). As the CeO_2 content increasing to the Cu_2Ce_8, all the satellite peaks disappear and the characteristic peak is observed at 932.1 eV which is the signal of low valence Cu characteristic peak.[37] However, the Cu 2p binding energy of Cu^+ and Cu^0 species is too difficult to distinguish, thus X-ray Cu LMM_a Auger lines is taken to identify the Cu valence (Cu^{2+}: 917.5 eV; Cu^+: 918.6 eV; Cu^0: 916.2 eV),[38,39] as shown in Fig. 6b. It can be seen that for the intergrowth and coexistence CuO-CeO_2 composite oxides, the Cu element mainly exists as the chemical state of Cu^{2+} when the Cu content is higher than Ce; on the contrary, the Cu element mainly exists as the chemical state of Cu^+ as the Cu content is lower than Ce, No Cu^0 specie is observed for all samples. The results indicate that Cu exists as the coexistence of Cu^{2+} and Cu^+ in the epiphase CuO structure for intergrowth CuO-CeO_2 samples. With the increase of CeO_2 content, the reduction reaction ($Cu^{2+} \rightarrow Cu^+$) is promoted and generating oxygen vacancy correspondingly. This lead to the imperfect structure $[Cu^{2+}_{1-x}Cu^+_x][O_{1-x/2}\square_{x/2}]$ on the epiphase CuO.

As we can see from Fig. 6c, it shows the epiphase Ce mainly exists as the chemical state of Ce^{4+}. The v′ and u′ peaks are the satellite peaks origining from the Ce^{3+} $3d_{5/2}$ and $3d_{3/2}$,[10] suggesting that there exist a few Ce^{3+} in the surface of samples leading to forming the imperfect structure $[Ce^{4+}_{1-\sigma}Ce^{3+}_{\sigma}][O_{2-\sigma/2}\square_{\sigma/2}]$ on the epiphase CeO_2. Furthermore, the Ce^{4+} characteristic peak of intergrowth and coexistence CuO-CeO_2 samples slightly shifts to higher binding energy with the increase of Cu content compared with pure CeO_2 (Table 2). It is inferred that during the intergrowth and coexistence process, a strong interaction between Cu and Ce exists. This resulted in turning the CeO_2 electronic structure slightly, in good agreement with the above results.

In order to study the O species on the surface, the O 1s spectra is shown in Fig. 6d. The first peak (O′ 529.6-528.9 eV) represents for lattice oxygen bonding with metal ion, and the O characteristic peak obviously shifts to lower binding energy with the increase of Ce content (Table 2). This finding suggests that the binding energy between O and ion gradually decrease, suggesting the O species is reduced more easily. The second peak (O′′ 531.5-532.9 eV) is assigned to chemical adsorption oxygen.[10,40] There are oxygen vacancies on the surface of samples, O adsorbs onto the surface and forms O_2^- ion.

3.5. O_2-TPD results

The O_2-TPD experiments are carried out to gain insight into the nature of the surface oxygen species possibly involved in redox reactions. According to the literature,[41] the desorption peaks at low temperatures (<400 °C) are generally ascribed to superficial oxygen species, they are weakly bound to the surface. As shown in Fig. 7, except for the pure CuO sample, all other samples display two prominent characteristic peaks centered at ca. 100 and 270 °C, respectively. The first peak is ascribed to the physically adsorbed O_2 species weakly bound to the surface, which are easily desorbed at low temperatures.[41,42] The second peak is associated with O_2^- species formed by the adsorbed O_2 on the surface vacancies.[41,42] It is in good agreement with the XPS results. The two desorption peaks need be investigated further, as they are likely to participate in the redox reactions. The information of these desorption peaks is summarized in Table 3 (semi quantitative analysis). The amount of O_2 (ad) species increases with the increase of CeO_2 content, it is likely to be related to the BET area. In generally, the larger specific surface area aids in adsorpting more O_2, which acts as physically adsorbed oxygen. However, the amount of O_2^- species increases significantly with the introduction of the CeO_2, that of Cu5Ce5 sample is the largest and then decreases. This result further testifies that the CuO-CeO_2 sample obtained in the work is an intergrowth and coexistence system, and there exist strong interactions between CuO and CeO_2. Resulting in high density of surface oxygen vacancy, which might play an important role in accelerating the activation and the formation of chemisorbed O_2^- species.

3.6. TG-DSC results

The thermal behavior of the Cu_5Ce_5 sample before heat treatment and the activate carbon are probed by performing TG analysis and DSC under air flow. A 7.3% mass loss on the TG curve before 220 °C accompanied by an exothermic peak centered at 203 °C on the DSC signal are observed in Fig. 8a, which should be attributed to desorption of chemically adsorbed hydroxyls on the surface of the sample and to the decomposition of lattice hydroxyls. The major endothermal peak centered at 242 °C accompanied by a mass loss of 25.7% is detected before 300 °C which is due to the decomposing of citric acid, and the mass loss continues until around 500 °C, which is attributed to the chemical decomposition of activate carbon probed by TG-DSC curves of the pure activate carbon (Fig. 8b).

3.7. Forming process of two phase intergrowth and coexistence CuO-CeO_2

$Cu(NO_3)_2$ and $Ce(NO_3)_3$ were taken as the precursors of CuO and CeO_2, an uniformly mixed aqueous salt solution containing Cu^{2+} and Ce^{3+} was prepared. Citric acid monohydrate (chelating agent) was then added to this solution, each of the citric acid has equal opportunity to chelate a Cu^{2+} and Ce^{3+} or two Cu^{2+} or two Ce^{3+}, forming citric acid metal chelate in the water. After that, the obtained solution was impregnated onto activate carbon. After being dried at 90 °C to remove the water, the citric acid metal chelate can distribute on the activate carbon uniformly. Citric acid decomposes into H_2O and CO_2 after pyrolysis at 230 °C. All Cu^{2+} and Ce^{3+} separate out in the form of exploding concurrently resulting in formation of copper or cerium oxide fine powder samples that are several Å magnitudes which are mixed uniformly. By this time, the copper oxide exists as CuO, the cerium oxide exists as $Ce^{4+}_{1-n}Ce^{3+}_{n}O_{2-n/2}$ and Ce^{3+} accounts for larger proportion resulting from that the Ce^{3+} is chelated by citric acid and rapidly separates out at the time of pyrolysis which gives rise to not all Ce^{3+} formation into Ce^{4+}.

At the second stage, the pyrolysis samples are activated at high temperature. By this time, on the one hand, the $Ce^{4+}_{1-n}Ce^{3+}_{n}O_{2-n/2}$ obtain some oxygen from the air resulting in part of Ce^{3+} formation into Ce^{4+}:

$$Ce^{4+}_{1-n}Ce^{3+}_{n}O_{2-n/2} + (1/4)zO_2 \rightarrow Ce^{4+}_{1-(n-z)}Ce^{3+}_{(n-z)}O_{2-(n-z)/2}$$

On the other hand, CeO_2 can also get some oxygen from the CuO to make Ce^{3+} form into Ce^{4+} in that the particles of CuO and CeO_2 are small, well-dispersive and contact closely:

$$CuO \rightarrow Cu^{2+}_{1-x}Cu^{+}_{x}O_{1-x/2} + (1/4)xO_2$$

$$Ce^{4+}_{1-(n-z)}Ce^{3+}_{(n-z)}O_{2-(n-z)/2} + (1/4)x\ O_2 \rightarrow Ce^{4+}_{1-(n-z-x)}Ce^{3+}_{(n-z-x)}O_{2-(n-z-x)/2}$$

Labeling (n-z-x)=σ, and the $Ce^{4+}_{1-(n-z-x)}$ $Ce^{3+}_{(n-z-x)}O_{2-(n-z-x)/2}$ can be reduced to $Ce^{4+}_{1-\sigma}Ce^{3+}_{\sigma}O_{2-\sigma/2}$.

The above structures also generate corresponding oxygen vacancies, consequently the constitutional formula of two phase intergrowth and coexistence CuO-CeO_2 after revitalite, respectively are as follows:

$$[Cu^{2+}_{1-x}Cu^{+}_{x}][O_{1-x/2}\square_{x/2}]$$

$$[Ce^{4+}_{1-\sigma}Ce^{3+}_{\sigma}][O_{2-\sigma/2}\square_{\sigma/2}]$$

The higher cerium oxide content is in the intergrowth CuO-CeO_2, the more oxygen of CeO_2 can get from the CuO, which leading to more Cu^+ and oxygen vacancies. However, although cerium oxide obtains oxygen from CuO, it can also get the oxygen from air to convert Ce^{3+} into Ce^{4+}, thus the CuO content has little effect on the CeO_2 structure. And the two phase intergrowth and coexistence process of CuO-CeO_2 finally shows that it has a major influence on CuO structure but little influence on CeO_2. This result is in good agreement with above XRD and XPS results. They show that for the two phase intergrowth and coexistence CuO-CeO_2 samples, with increasing CeO_2 content, the epiphase Cu^+ content increases (XPS result) and also the cell volume of CuO phase increases (XRD result, Cu^{2+}=0.72 Å, Cu^+=0.96 Å). Hence both epiphase and bulk-phase of CuO are imperfect structure. Moreover, Cu exists as the coexistence

of Cu^{2+} and Cu^{+} probability and generating oxygen vacancy correspondingly; the cell volume of CeO_2 phase has relatively little change and has nothing to do with CuO content.

3.8. H_2-TPR results

The reduction properties of Cu_mCe_n and Cu_mCe_n-M samples were characterized by H_2-TPR, and results are shown in Fig. 9. Detailed information of the reduction peaks obtained is also summarized in Table 3. All the peaks are of CuO reduction peak, no reduction peak can be seen for CeO_2 indicating that CeO_2 cannot be reduced in the temperature range of the 100-400 °C. It is worth noting that for the intergrowth and coexistence CuO-CeO_2 samples (Fig. 9a), the temperature of the CuO reduction peaks are obviously lower than that of pure CuO (245 °C), and the more CeO_2, the larger degree it shifts toward lower temperature (from 187 to 126 °C). This finding illustrates that the intergrowth and coexistence effect significantly improves the redox ability of CuO. For comparison, Fig. 9b shows the TPR profiles of Cu_mCe_n-M samples. The CuO reduction peaks of Cu_mCe_n-M and Cu_mCe_n samples are quite similar to each other. The reduction peaks almost maintain at 245 °C and do not shift along with increasing CeO_2. However, for the Cu_mCe_n-M samples, a small shoulder peak is observed at low temperature besides that of an extremely strong peak observed at the CuO reduction peak. Two of them are assigned to the reduction of small (close contact with CeO_2) and large particles, respectively, a few parts of small particles and large particles have already been observed from SEM and EDX. The results are attributed to the simple mixture of CuO and CeO_2 for the Cu_mCe_n-M samples; they have scarcely interaction between CuO and CeO_2. This phenomenon indicates, for the Cu_mCe_n samples, a strong interaction between CuO and CeO_2 phases lead to the improved redox reduction, suggesting this is an intergrowth system and it is obviously different from that mechanical mixture.

To further explore the influence of adding CeO_2 on Cu_mCe_n, the peak areas of the Cu_mCe_n TPR profiles have been integrated (as shown in Table 3). It can be observed that the ratio of theoretical consumption (T) and actual H_2 consumption (A) is close to 1.0 but larger than 1.0, suggesting most of the reduction peak areas come from the reduction of CuO, and CeO_2 does not take part in the reaction. In addition, it indicates that low valence Cu^{+} exists in the samples giving rise to the decrease of actual H_2 consumption. The result is in agreement with the XPS results.

3.9. Oxygen Storage Capacity

Fig. 10 shows the OSC values of Cu_mCe_n and Cu_mCe_n-M samples as a function of the molar ratio Ce/(Ce+Cu). It can be observed that a small quantity of CeO_2 adding can significantly increase the OSC value which is approximately three times compared with pure CuO (400 μmol/g). The OSCs of the Cu_mCe_n samples increase with increasing CeO_2 amount at n≤3 and slowly decreases at n>3, but dramatically reduces when n=8. Increase in OSC with increasing CeO_2 amount depends on the number of oxygen vacancies in the sample, which, in turn, affects oxygen mobility within the CuO network. The more CeO_2 content, the more Cu^{+} content according to XPS results, and the more Cu^{+} content, the more vacancies according to the $[Cu^{2+}_{1-x}Cu^{+}_{x}][O_{1-x/2}\square_{x/2}]$. As a result, there are excesses in vacancy density, which leads to stable vacancy-dopant cation association[43,44] and limits the number of mobile vacancies. Consequently, beyond the limit of about n=3, the OSC decreases gradually. The sample Cu_7Ce_3 shows a maximum OSC of 1305 μmol/g; By contrast, the varying pattern of OSC for Cu_mCe_n-M is similar to the Cu_mCe_n, however, the OSC values of Cu_mCe_n-M are distinctly lower than the corresponding Cu_mCe_n, indicating the OSC of two phase intergrowth and coexistence Cu_mCe_n is superior.

According to the above characterizations, the high OSC of CuO-CeO_2 may be attributed to the effect of two phase intergrowth and coexistence, CuO and CeO_2 form a uniform intergrowth system in which strong interactions between the components exist; These interactions induce CeO_2 lattice distortions (HRTEM results) not only produces more lattice defects and oxygen vacancies, but also decrease the stability between vacancy and dopant cation and increase the number of mobile vacancies, thus enhance in OSC greatly achieve. While the Cu_mCe_n-M samples are obtained only by mixing mechanically CuO and CeO_2, without a symbiotic process, they have no strong interaction between CuO and CeO_2. Consequently, Cu_mCe_n samples with a certain amount of CeO_2 show significantly enhanced OSC. It can be inferred that the intergrowth play a major role for the enhanced OSC. The results are in good agreement with XPS and HRTEM results, and further prove the forming process of two phase intergrowth and coexistence CuO-CeO_2.

3.10. Catalytic activity for CO oxidation

The T_{50} and T_{90} curves of Cu_mCe_n and Cu_mCe_n-M samples with different molar ratios are shown in Fig. 11. According to the Fig. 11a, the T_{50} of intergrowth Cu_mCe_n is clearly lower than pure CuO and gently decreases with the increase of CeO_2. Yet the T_{50} of Cu_mCe_n-M is far higher than the matching Cu_mCe_n and it further increases with the increase of CeO_2, in addition, active constituent of CuO decreases. For the T_{90} (Fig. 11b), the varying pattern of each sample is in agreement with the T_{50}. The intergrowth Cu_mCe_n samples prepared in this work show excellent catalytic activity for CO oxidation, the T_{50} and T_{90} of Cu_2Ce_8 reach 87 °C and 104 °C, respectively, which is much lower than that of literatures.[16,38,45] The result is attributed to the strong interactions producing during the intergrowth process, leading to forming $[Cu^{2+}_{1-x}Cu^{+}_{x}][O_{1-x/2}\square_{x/2}]$ with imperfect structure. Moreover, the low valence Cu^{+} and oxygen vacancy are contributed to the catalytic oxidation of CO.

3.11. Catalytic activity for NO reduction

As shown in Table 4 and Fig. 12, for pure CuO, the conversion and selectivity of NO reduction by CO have respectively been up to 100% and 77.7% at 220 °C which is far higher than pure CeO_2 (65.3% and 20.0%). However, there still are 22.3% NO that are converted into toxic N_2O. All the conversion and selectivity of the intergrowth CuO-CeO_2 sample have been up to 100% at 220 °C, which is much lower than the temperature value of CuO/CeO_2 catalyst ($T_{100\%}$=300 °C).[15,19] The high catalytic activity is attributed to the intergrowth and coexistence effect, making the CuO phase form $[Cu^{2+}_{1-x}Cu^{+}_{x}][O_{1-x/2}\square_{x/2}]$ in which the Cu^{+}_{x} and $\square_{x/2}$(oxygen vacancy) are favorable for absorbing CO and NO,[46,47] as a result, the reduction completely generating CO_2 and N_2 is promoted. With the increase of CeO_2 in the intergrowth CuO-CeO_2 sample, on the one hand, the amount of CuO with high activity decreases which has disadvantage of catalytic reduction reaction. However, on the other hand, it can increase the intergrowth and coexistence effect to increase the amounts of Cu^{+} and oxygen vacancies which are contributed to the catalytic reduction reaction. It is the combination of them that makes the Cu_5Ce_5 still retains high catalytic reduction activity.

3.12. CO or/and NO interaction with Cu9Ce1 catalyst

In order to further understand the nature of redox reactions over these samples, *in situ* DRIFTS technique is carried out. Fig. 13a exhibits the CO adsorption *in situ* DRIFTS spectra of Cu9Ce1 catalyst. The characteristic band associated with adsorbed CO molecules appears at ~2104 cm^{-1} at 50 °C, and strengthens at 100 °C, but decreases greatly at 150 °C and disappears when the temperature increases to 250 °C. Considering our previous investigation,[41,42] this band should be due to the linear CO-Cu^+ species formed by CO molecules adsorbed on Cu^+ sites and the reduction of Cu^+ ions to Cu^0 results in the disappearance of adsorption on Cu^+. Simultaneously, two clearly observable new peaks at 2337 and 2361 cm^{-1} are present at 100 °C, which is attributed to the formation of gaseous CO_2. Moreover, they are found to increase significantly with temperature as a result of the very likely catalyst reduction.

The NO adsorption *in situ* DRIFTS spectra of Cu9Ce1 catalyst have been recorded, as shown in Fig. 13b. The two peaks appear at 50 °C, assigned to characteristic vibrations of NO_3^- species, i.e., ν (N=O) of bridged bidentate NO_3^- (1488-1544 cm^{-1}) and chelated bidentate NO_3^- (1278-1295 cm^{-1}) respectively.[48] Some interesting results can be obtained during the heating procedure the adsorbed bridged bidentate NO_3^- at 1295 cm^{-1} gradually red shifts to 1278 cm^{-1}. Correspondingly, the chelated bidentate NO_3^- at 1488 cm^{-1} blue shifts to 1544 cm^{-1} and disappears at 150 °C. This phenomenon suggests that both bridged bidentate NO_3^- and chelated bidentate NO_3^- are not thermally stable and readily to decompose. For these phenomena, Dong et al[49] proposed a reasonable explanation that the surface oxygen vacancies form in Cu9Ce1 catalyst and favor NO dissociation. In addition, for whole temperature region, the two peaks at 1847 and 1901 cm^{-1} appear which are attributed to the gaseous NO.

The nature and population of the adsorbed NOx/COx species are identified by *in situ* DRIFTS spectra under simulated reaction conditions, with the purpose of further understanding the reaction progress for the synthesized samples. The NO and CO co-adsorption *in situ* DRIFTS spectra of Cu9Ce1 catalyst have been recorded, as shown in Fig. 13c. After exposure the catalyst to the reactants mixture at room temperature, NO preferentially interacts with the catalyst and forms NO_3^- species, with increasing the temperature, the bands change is agree with that of NO adsorption. However, No CO adsorption peak appears unless the gaseous CO peak appears at 2181 and 2112 cm^{-1}. When the temperature reach at 150 °C, the gaseous CO peak disappears, simultaneously, the peak associated with CO molecules adsorbed on Cu^+ sites (2121 cm^{-1}) appears. At higher adsorption temperatures (>150 °C), the CO-Cu^+ peak diminishes significantly and finally vanishes. In addition, the characteristic peaks associated with gaseous N_2O molecules appears at 2205 and 2237 cm^{-1} at 150 °C, remains constant below 250 °C, but decreases greatly when the temperature increases to 250 °C. It seems reasonable to explain the surface oxygen vacancies could induce NO dissociation to form O and N and then the dissociated N atom would recombine NO ($N+NO \rightarrow N_2O$).[49] Furthermore, N_2O species are intimately related to the catalytic selectivity. When the temperature increases to 225 °C, the process associating with the dissociation and recombination of NO to N_2 causes an increase in N_2 selectivity.

According above results, the possible reaction mechanisms are tentatively proposed for the CO oxidation and NO+CO reactions. For the CO oxidation reaction, the adsorbed CO molecules on Cu^+ can react with the O_2^- species formed by the adsorption of O_2 on the oxygen vacancy to produce small amounts of CO_2. For the NO+CO reaction, at the low temperature, the surface oxygen vacancies could induce NO dissociation to form O and N, which react with CO gas to produce CO_2+N_2O. With the increase of temperature, the dissociated NO react with the adsorbed CO molecules on Cu^+ to produce CO_2+N_2.

Conclusions

The Cu_mCe_n composite oxide powders were synthesized by an improved IACP method. The as-prepared catalyst is an intergrowth and coexistence system which consists of imperfect monoclinic crystal CuO and cubic crystal CeO_2. Strong intergrowth interactions are generated during the intergrowth process, making that some Cu^{2+} species of CuO gradually form Cu^+ and produce corresponding oxygen vacancy resulting in the $[Cu^{2+}_{1-x}Cu^+_x][O_{1-x/2}\square_{x/2}]$ with imperfect structure, which is contributed to absorbing reaction species, and make the relevant reaction successfully take place.

As a result, the oxygen storage capacity (the highest OSC is 1305 μmol/g), CO oxidation activity and catalytic redox performance of CO and NO are greatly enhanced. Both NO conversion and N_2 selectivity have reached 100% at 220 °C. The results are explained by taking into account the intergrowth and coexistence effects of CuO-CeO_2. The possible reaction mechanisms are tentatively proposed for the CO oxidation and NO+CO reactions. Cu^+ species can adsorb CO molecules and the oxygen vacancy can adsorb O_2 and induce NO dissociation to form O and N.

Acknowledgements

The financial supports of National Basic Research Program of China (973 program, No. 2012CB21500203)

References

1 X. J. Yao, L. Zhang, L. L. Li, L. C. Liu, Y. Cao, X. Dong, F. Gao, Y. Deng, C. J. Tang, Z. Chen, L. Dong and Y. Chen, *Appl. Catal. B: Environ.,* 2014, **150-151**, 315-329.

2 A. A. Gokhale, J. A. Dumesic and M. Mavrikakis, *J. Am. Chem. Soc.,* 2008, **130**, 1402-1414.

3 L. L. Wang, L. M. Yang, Y. H. Zhang, W. Ding, S. P. Chen, W. P. Fang and Y. Q. Yang, *Fuel Process Technol.*, 2010, **91**, 723-728.

4 X. D. Ma, X. Feng, X. He, H. W. Guo, L. Lv, J. Guo, H. Q. Cao and T. Zhou, *Micropor. Mesopor. Mat.,* 2012, **158**, 214-218.

5 X. C. Zheng, X. L. Zhang, X. Y. Wang, S. R. Wang and S. H. Wu, *Appl. Catal. A: Gen.,* 2005, **295**, 142-149.

6 S. S. Maluf, P. A. P. Nascente and E. M. Assaf, *Fuel Process. Technol.,* 2010, **91**, 1438-1445.

7 L. Qi, Q. Yu, Y. Dai, C. J. Tang, L. J. Liu, H. L. Zhang, F. Gao, L. Dong and Y. Chen, *Appl. Catal. B: Environ.,* 2012, **119-120,** 308-320.

8 A. Martínez-Arias, A. B. Hungría, A. Iglesias-Juez, M. Fernández-García, J. A. Anderson, J. C. Conesa, G. Munuera and J. Soria, *Catal. Today,* 2012, **180**, 81-87.

9 C. Y. Lu, W. C. Chang and M. Y. Wey, *Mater. Chem. Phys.,* 2013, **141**, 512-518.
10 S. H. Zeng, W. L. Zhang, M. C. Sliwa and H. Q. Su, *Int. J. Hydrogen Energy,* 2013, **38**, 3597-3605.
11 G. X. Chen, Q. L. Li, Y. C. Wei, W. P. Fang and Y. Q. Yang, *J. Chem.,* 2013, **34**, 322-329.
12 D. Gamarra, A. López-Cámara, M. Monte, S. B. Rasmussen, L. E. Chinchilla, A. B. Hungría, G. Munuera, N. Gyorffy, Z. Schay, V. Cortés-Corberán, J. C. Conesa and A. Martínez-Arias, *Appl. Catal. B: Environ.,* 2013, **130-131**, 224-238.
13 S. Y. Yao, K. Mudiyanselage, W. Q. Xu, A. C. Johnston-Peck, J. C. Hanson, T. P. Wu, D. Stacchiola, J. A. Rodriguez, H. Y. Zhao, K. A. Beyer, K. W. Chapman, P. J. Chupas, A. Martínez-Arias, R. Si, T. B. Bolin, W. J. Liu and S. D. Senanayake, *ACS Catal.,* 2014, **4**, 1650-1661.
14 S. H. Zeng, Y. Wang, S. P. Ding, J. J. H. B. Sattler, E. Borodina, L. Zhang, B. M. Weckhuysen and H. Q. Su, *J. Power Sources,* 2014, **256**, 301-311.
15 J. F. Chen, J. J. Zhu, Y. Y. Zhan, X. Y. Lin, G. H. Cai, K. M. Wei and Q. Zheng, *Appl. Catal. A: Gen.,* 2009, **363**, 208-215.
16 J. M. Zamaro, N. C. Perez, E. E. Miro, C. Casado, B. Seoane, C. Tellez and J. Coronas, *Chem. Eng. J.,* 2012, **195-196,** 180-187.
17 E. Morettia, L. Storaro, A. Talon, P. Riello, A. I. Molina and E. Rodriguez-Castellon, *Appl. Catal. B: Environ.,* 2015, **168-169**, 385-395.
18 A. P. Jia, S. Y. Jiang, J. Q. Lu, and M. F. Luo, *J. Phys. Chem. C,* 2010, **114**, 21605-21610.
19 X. J. Yao, F. Gao, Q. Yu, L. Qi, C. J. Tang, L. Dong and Y. Chen, *Catal. Sci. Technol.,* 2013, **3**, 1355-1366.
20 S. C. Hayden, N. K. Allam and M. A. El-Sayed, *J. Am. Chem. Soc.,* 2010, **132**, 14406-14408.
21 H. Kim, J. Kim, W. Kim and W. Choi, *J. Phys. Chem. C,* 2011, **115**, 9797-9805.
22 R. Dagani, *Chem. Eng. News,* 1999, **77**, 25-25.
23 G. M. Schwab and E. Pietsch, *Z. Phys. Chem.,* 1928, **1**, 386-408.
24 G. M. Schwab and E. Pietsch, *Z. Phys. Chem.,* 1929, **35**, 135-141.
25 G. M. Schwab, E. Pietsch and E. Josephy, *Z. Phys. Chem.,* 1931, **37**, 666-670.
26 E. Pietsch, A. Kotowski and G. Berend, *Z. Phys. Chem.,* 1929, **35**, 582-586.
27 M. N. Huang, J. H. Yu, B. Li, C. S. Deng, L. Wang, W. K. Wu, L. H. Dong, F. Y. Zhang and M. G. Fan, *J. Alloys Compd.,* 2015, **629**, 55-61.
28 B. Li, S. Li, Y. Wang, N. Li, W. Zhang, B. X. Lin, Chin. *J. Catal.,* 2010, **31**, 528-534.
29 B. Li, G. Z. Jin, J. B. Gao, R. S. Zhao, L. H. Dong, Y. J. Gong, *CrystEngComm,* 2014, **16**, 1253-1256.
30 N. Li, X. Xu, D. Luo, Y. S. Wu, S. J. Li, B. X. Lin, *J. Power Sources,* 2004, **126**, 229-235.
31 N. Li, X. M. Yan, W. J. Zhang, B. X. Lin, *J. Power Sources,* 1998, **74**, 255-258.
32 M. N. Huang, S. H. Yu, B. Li, L. H. Dong, F. Y. Zhang, M. G. Fan, L. Wang, J. H. Yu, C. S. Deng, *Ceram. Int.,* 2014, **40**, 13305-13312.
33 C. Marcilly, P. Courty, B. Delmon, *J. Am. Ceramic Soc.,* 1970, **53**, 56-57.
34 O. Y. Jing, H. M. Yang, *J. Phys. Chem. C,* 2009, **113**, 6921-6928.
35 E. Wu. POWD MULT; An Interactive Powder Diffraction Data Interpretation and Indexing Program. Version 2.1 School of Physical Sciences. Flinder University of South Australia. Bardford Park. SA. Australia. 1989.
36 Y. K. Tovbin, Theory of Physical Chemistry Processes at a Gas-Solid Interface, Boston London: CRD Press, 1911, 11.
37 C. Z. Sun, J. Zhu, Y. Y. Lv, L. Qi, B. Liu, F. Gao, K. Q. Sun, L. Dong and Y. Chen, *Appl. Catal. B: Environ.,* 2011, **103**, 206-222.
38 G. Avgouropoulos, T. Ioannides, *Appl. Catal. A: Gen.,* 2003, **244**, 155-167.
39 Y. Tanaka, R. Kikuchi, T. Takeguchi, K. Eguchi, *Appl. Catal. B: Environ.,* 2005, **57**, 211-222.
40 L. Qi, Q. Yu, Y. Dai, C.J. Tang, L.J. Liu, H.L. Zhang, F. Gao, L. Dong and Y. Chen, *Appl. Catal. B: Environ.,* 2012, **119-120**, 308-320.
41 L. H. Dong, Y. X. Tang, B. Li, L. Y. Zhou, F. Z. Gong, H. X. He,B. Z. Sun, C. J. Tang, F. Gao and L. Dong, *Appl. Catal. B: Environ.,* 2016, **180**, 451-462.
42 C. S. Deng, B. Li, L.H. Dong, F. Y. Zhang, M. G. Fan, G. Z. Jin, J. B. Gao, L. W. Gao, F. Zhang and X. P Zhou, *Phys. Chem. Chem. Phys.*, 2015, **17**, 16092-16109.
43 B. M. Reddy, L. Katta and G. Thrimurthulu, *Chem. Mater.,* 2010, **22**, 467-475.
44 O. Toyo, Y. Satoshi, T. Tatsuya, A. Yuji, M. Tsuneo, H. Taikan and K. Katsumi, *Solid State Ionics,* 1998, **113**, 559-564.
45 A. Martínez-Arias, M. Fernández-García, O. Gálvez, J. M. Coronado, J. A. Anderson, J. C. Conesa, J. Soria, and G. Munuera, *J. Catal.*, 2000, **195**, 207-216.
46 X. J. Yao, Y. Xiong, W. X. Zou, L. Zhang, S. G. Wu, X. Dong, F. Gao, Y. Deng, C. J. Tang, Z. Chen, L. Dong and Y. Chen, *Appl. Catal. B: Environ.,* 2014, **144**, 152-165.
47 X. J. Yao, Q. Yu, Z. Y. Ji, Y. Y. Lv, Y. Cao, C. J. Tang, F. Gao, L. Dong and Y. Chen, *Appl. Catal. B: Environ.,* 2013, **130-131**, 293-304.
48 L. H. Dong, L. L. Zhang, C. Z. Sun, W. J. Yu, J. Zhu, L. J. Liu, B. Liu, Y. H. Hu, F. Gao, L. Dong and Y. Chen, *ACS Catal.*, 2011, **1,** 468-480.
49 D. Li, Q. Yu, S. S. Li, H. Q. Wan, L. Qi, B. Liu, F. Gao and L. Dong. *Chem. Eur. J.*, 2011, **17**, 5668-5679.

Table 1 The crystal lattice parameters of CeO_2 phase and CuO phase of the Cu_mCe_n samples.

Samples	CuO					CeO_2	
	a(Å)	b(Å)	c(Å)	β	V(Å^3)	a(Å)	V(Å^3)
CuO	4.6900(2)[a]	3.4266(1)[a]	5.1350(2)[a]	99.474(9)[a]	81.397		
Cu_9Ce_1	4.6900(2)	3.4269(1)	5.1356(2)	99.511(8)	81.405	5.4172(2)[a]	158.97
Cu_8Ce_2	4.6899(2)	3.4266(1)	5.1367(2)	99.489(8)	81.418	5.4173(2)	158.98
Cu_7Ce_1	4.6918(2)	3.4270(1)	5.1335(2)	99.438(8)	81.423	5.4173(2)	158.98
Cu_6Ce_4	4.6911(2)	3.4271(1)	5.1355(2)	99.467(9)	81.440	5.4174(2)	158.99
Cu_5Ce_5	4.6923(2)	3.4291(1)	5.1326(2)	99.495(8)	81.453	5.4180(2)	159.05
Cu_4Ce_6	4.6917(2)	3.4299(1)	5.1329(2)	99.488(9)	81.468	5.4176(2)	159.01
Cu_3Ce_7	4.6916(2)	3.4268(1)	5.1382(2)	99.498(8)	81.475	5.4182(2)	159.06
Cu_2Ce_8	4.6953(2)	3.4271(1)	5.1343(2)	99.460(8)	81.494	5.4167(2)	158.93
Cu_1Ce_9	4.7012(2)	3.4266(1)	5.1277(2)	99.330(8)	81.510	5.4175(2)	159.00
CeO_2						5.4182(2)	159.06

[a] The estimated standard deviation

Table 2 The binding energy (eV) of Cu_mCe_n samples.

Samples	O1s	Cu $2p_{3/2}$	Cu $2p_{1/2}$	Ce $3d_{5/2}$(V)	Ce $3d_{3/2}$(U^{III})
CuO	529.6	933.6	953.4		
Cu_9Ce_1	529.5	933.2	953.2	882.3	916.6
Cu_8Ce_2	529.3	932.8	952.7	882.1	916.4
Cu_7Ce_3	529.4	932.9	952.8	882.3	916.6
Cu_6Ce_4	529.2	932.5	952.2	882.1	916.4
Cu_5Ce_5	529.2	932.4	952.1	882.1	916.4
Cu_4Ce_6	529.3	932.4	952.3	882.1	916.5
Cu_3Ce_7	529.1	932.1	951.7	882.0	916.3
Cu_2Ce_8	529.2	932.1	951.7	882.1	916.4
Cu_1Ce_9	529.1	932.1	951.7	882.0	916.3
CeO_2	528.9			881.7	916.0

Table 3 The peaks areas of the H_2-TPR and O_2-TPD profiles, and the H_2 consumption (mmol/g) of the Cu_mCe_n samples.

Samples	Peak area (100~400 °C)	H_2-TPR results Theoretical H_2 consumption (mmol/g)	Actual H_2 consumption (mmol/g)	T/A	O_2-TPD results Area of the first peaks (~100 °C)	Area of the second peaks(~270 °C)
CuO	57403.07	12.57	12.57	1.00	129	149
Cu_9Ce_1	45226.84	10.13	9.90	1.02	318	212
Cu_8Ce_2	34560.01	8.16	7.57	1.08	529	238
Cu_7Ce_3	26441.81	6.52	5.79	1.13	749	276
Cu_6Ce_4	20015.41	5.15	4.38	1.18	1050	428.
Cu_5Ce_5	13863.54	3.97	3.04	1.31	1126	1140
Cu_4Ce_6	11526.16	2.96	2.52	1.17	1186	888
Cu_3Ce_7	8259.37	2.08	1.81	1.15	1401	836
Cu_2Ce_8	5643.82	1.30	1.24	1.05	1514	672
Cu_1Ce_9	2474.35	0.61	0.54	1.13	1581	570
CeO_2	397.34				1941	571

Table 4 The experimental data of CO catalytic reduction of NO of Cu_mCe_n samples at 220 °C.

Samples	NO conversion α%	N_2 seletivity β%	CO conversion γ%
CuO	100	77.7	53.4
Cu_9Ce_1	100	100	54.2
Cu_8Ce_2	100	90.2	49.3
Cu_7Ce_3	100	87.0	48.5
Cu_6Ce_4	100	100	53.2
Cu_5Ce_5	100	91.1	46.8
Cu_4Ce_6	100	85.2	44.5
Cu_3Ce_7	98.1	80.8	40.5
Cu_2Ce_8	97.5	65.0	32.2
Cu_1Ce_9	83.7	65.8	32.9
CeO_2	65.3	20.0	14.5

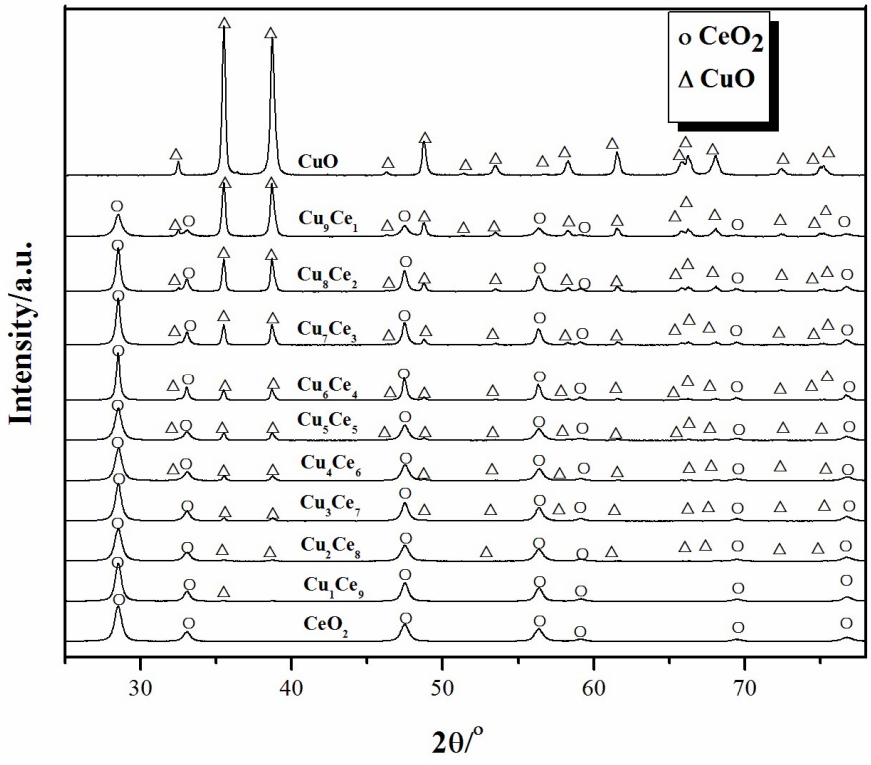

Figure 1. XRD patterns of the Cu_mCe_n samples with different Cu:Ce molar ratios.

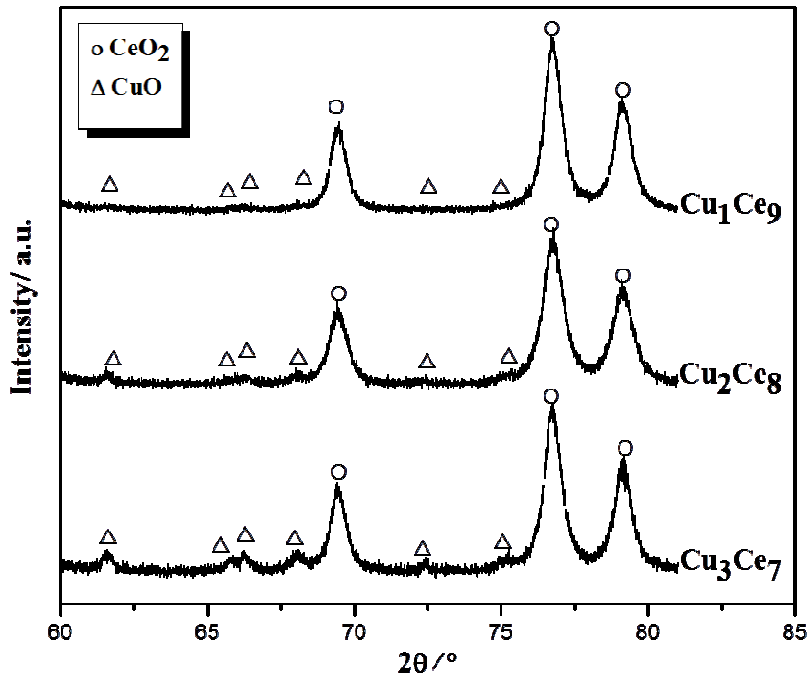

Figure 2. XRD patterns of the Cu_3Ce_7, Cu_2Ce_8, and Cu_1Ce_9.

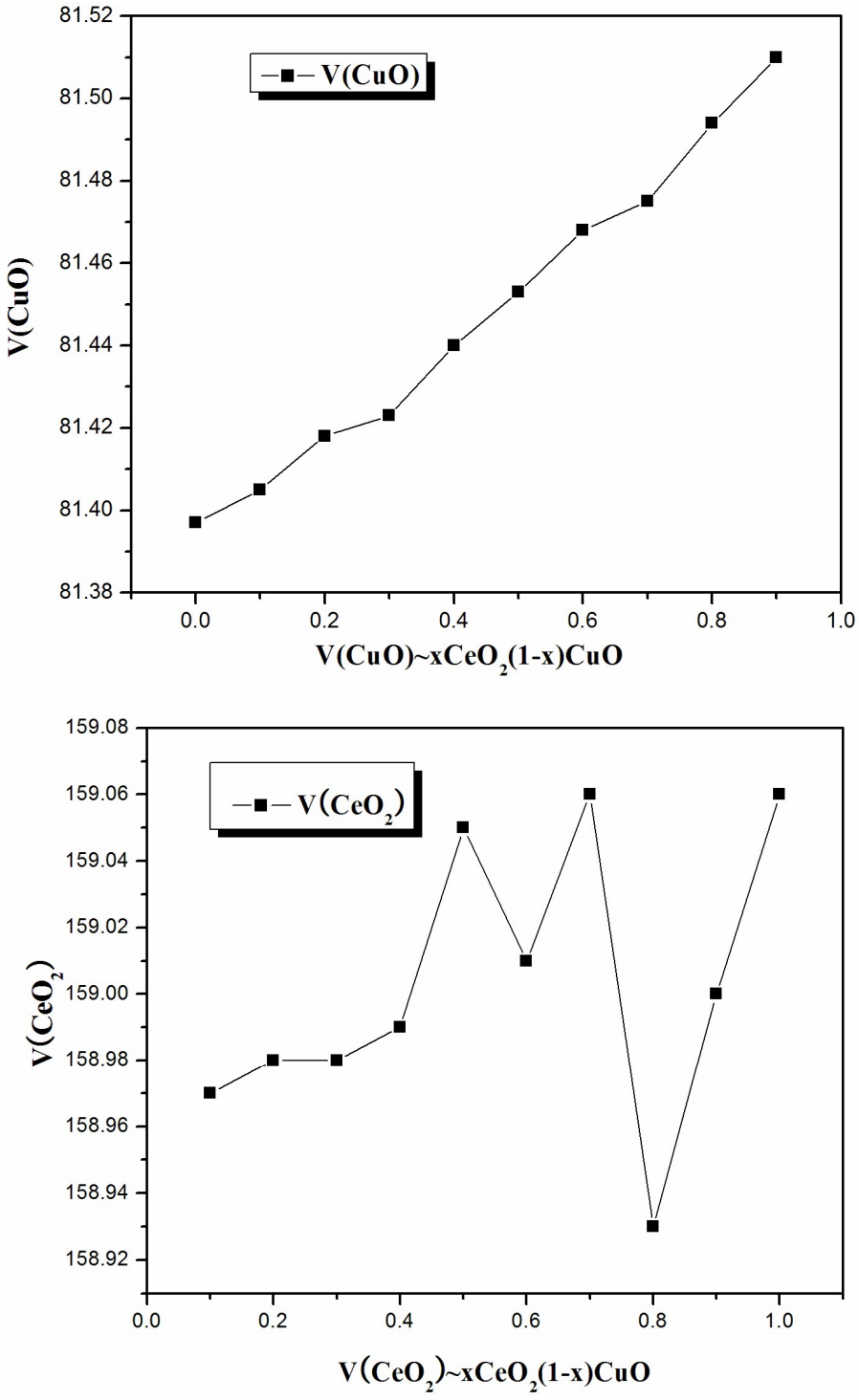

Figure 3. The change of cell volume of CeO_2 phase and CuO phase of the Cu_mCe_n

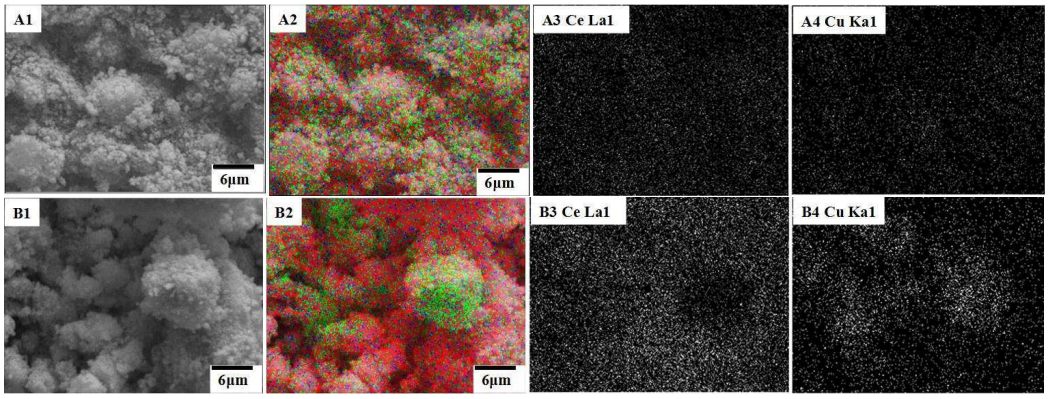

Figure 4. The EDX mapping result of the Cu_6Ce_4 sample: (A1) SEM image; (A2) Mixture signal; (A3) Ce signal; (A4) Cu signal and the mechanical mixture of Cu_6Ce_4-M sample: (B1) SEM image; (B2) Mixture signal; (B3) Ce signal; (B4) Cu signal.

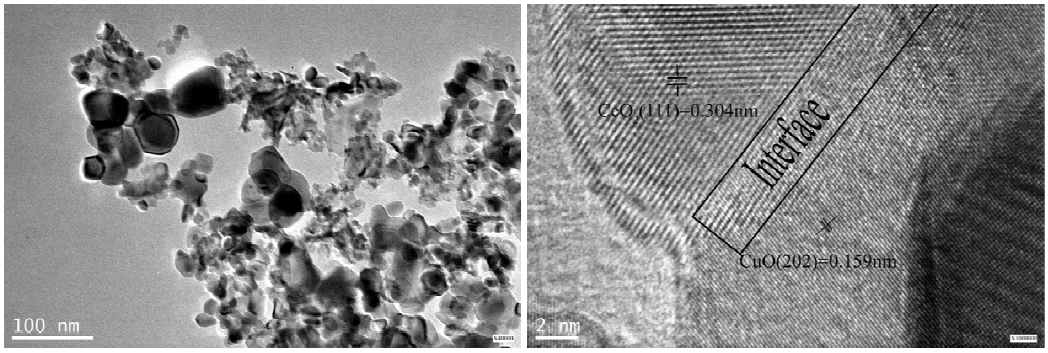

Figure 5. TEM and HRTEM images of the Cu_5Ce_5 catalyst.

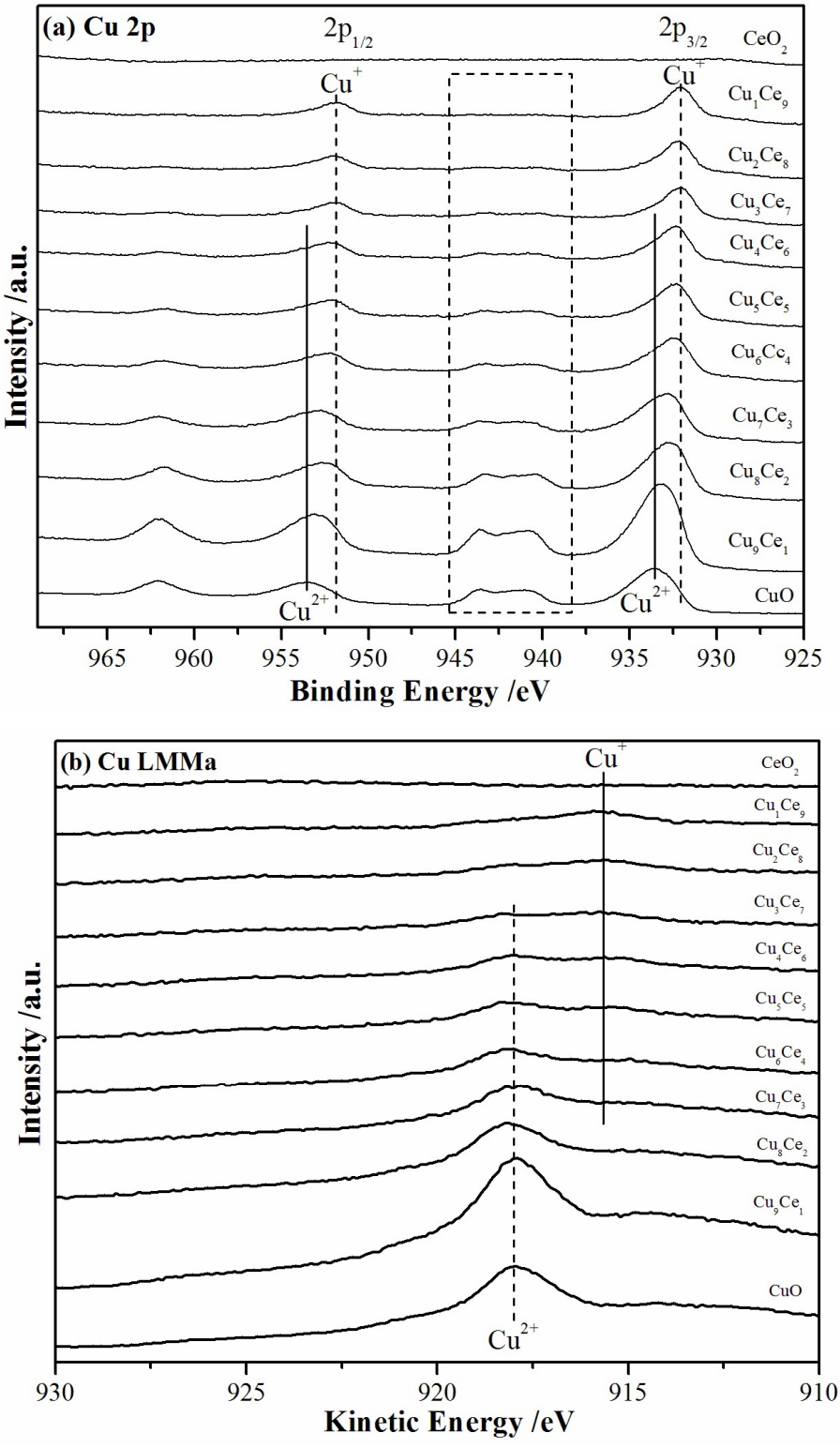

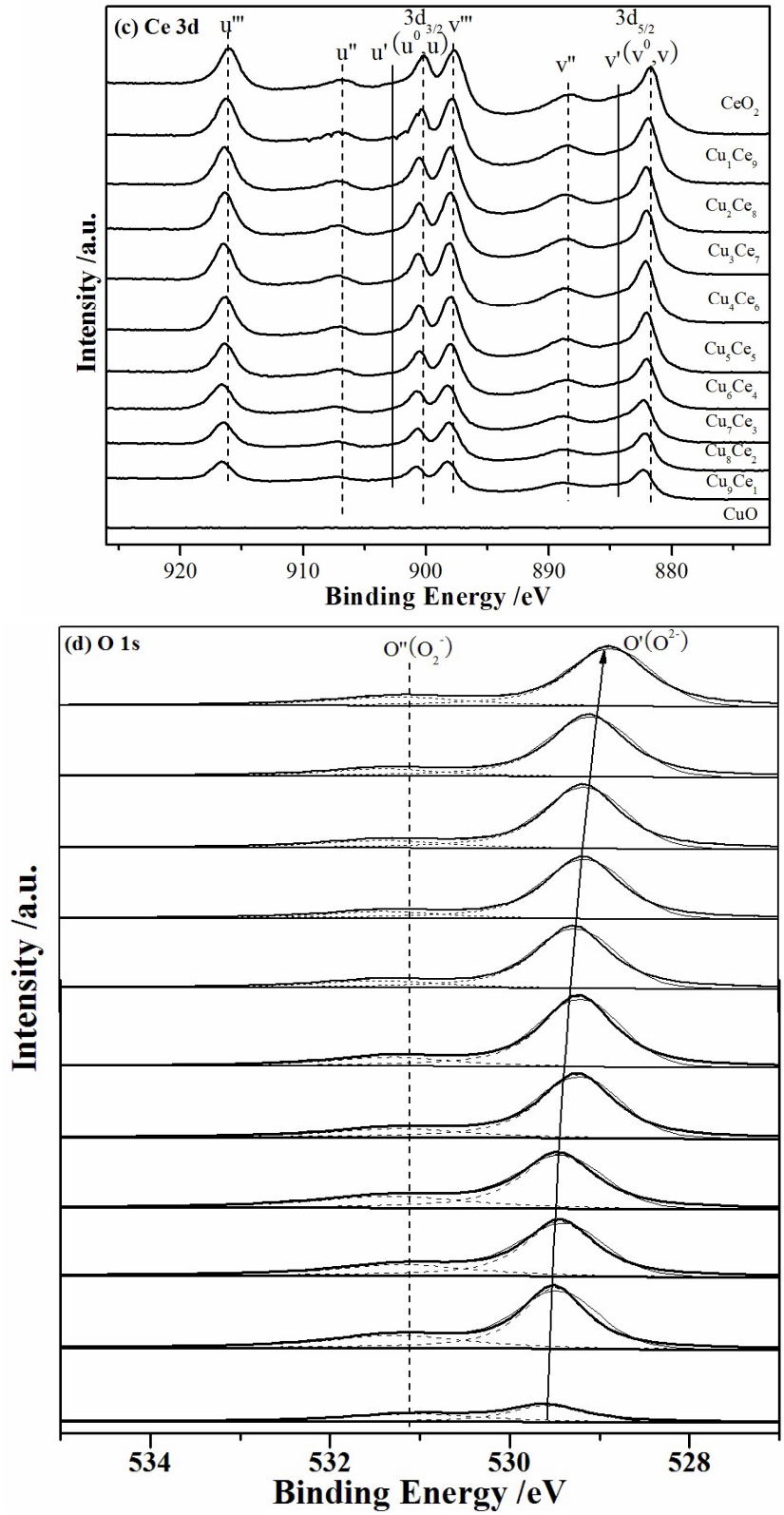

Figure 6. XPS spectra of the CuO-CeO_2 samples with different Cu:Ce molar ratios.

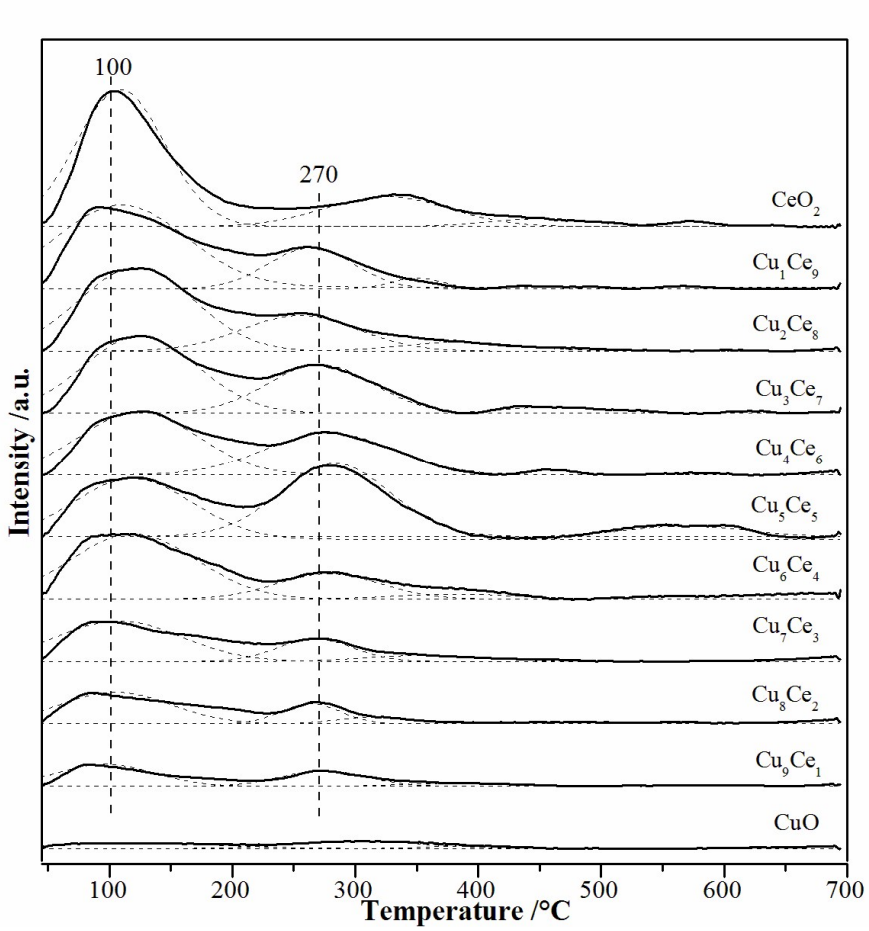

Figure 7. O_2-TPD profiles of these catalysts.

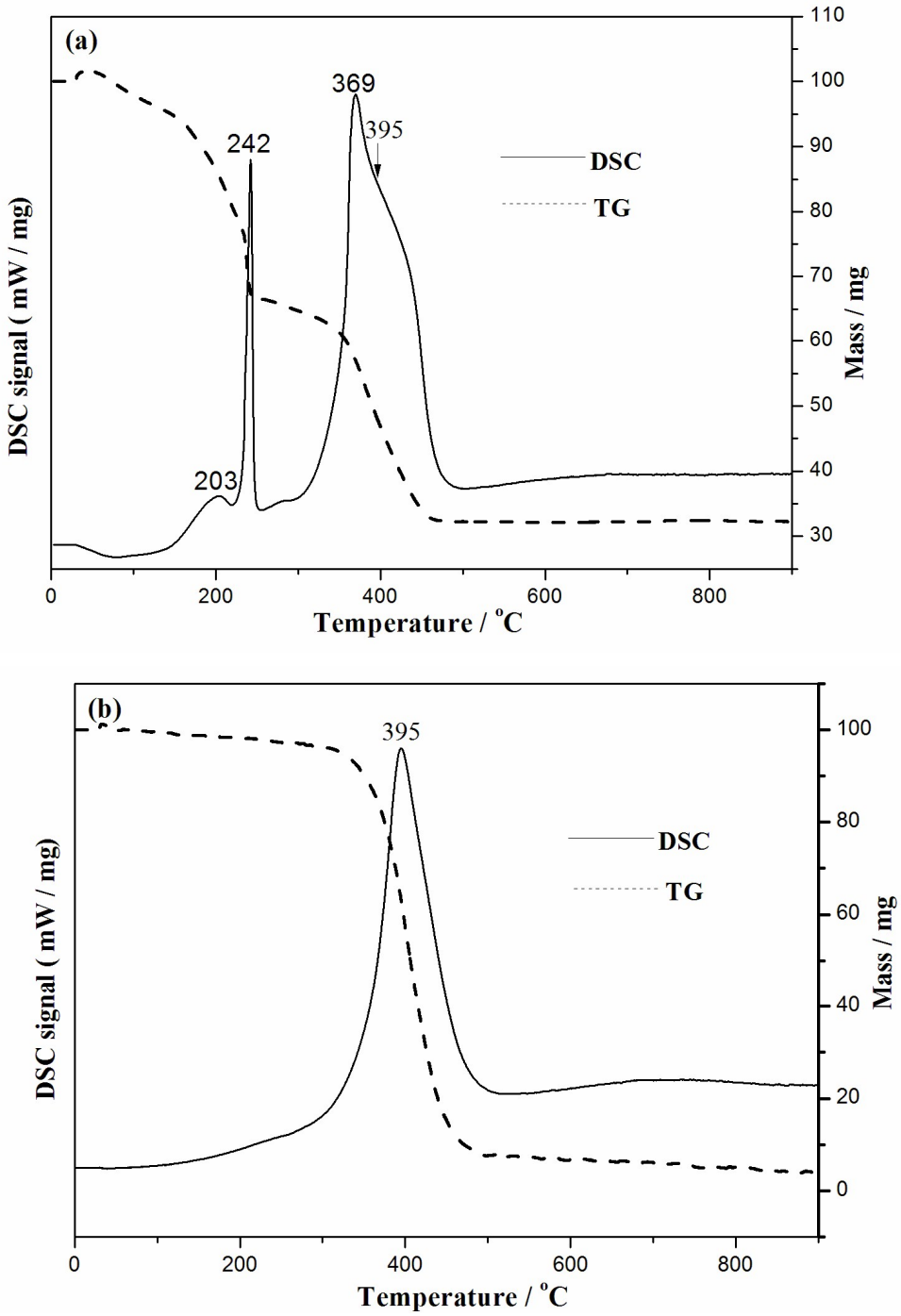

Figure 8. TG-DSC curves of the Cu_5Ce_5 sample before heat treatment (a) and the activate carbon (b).

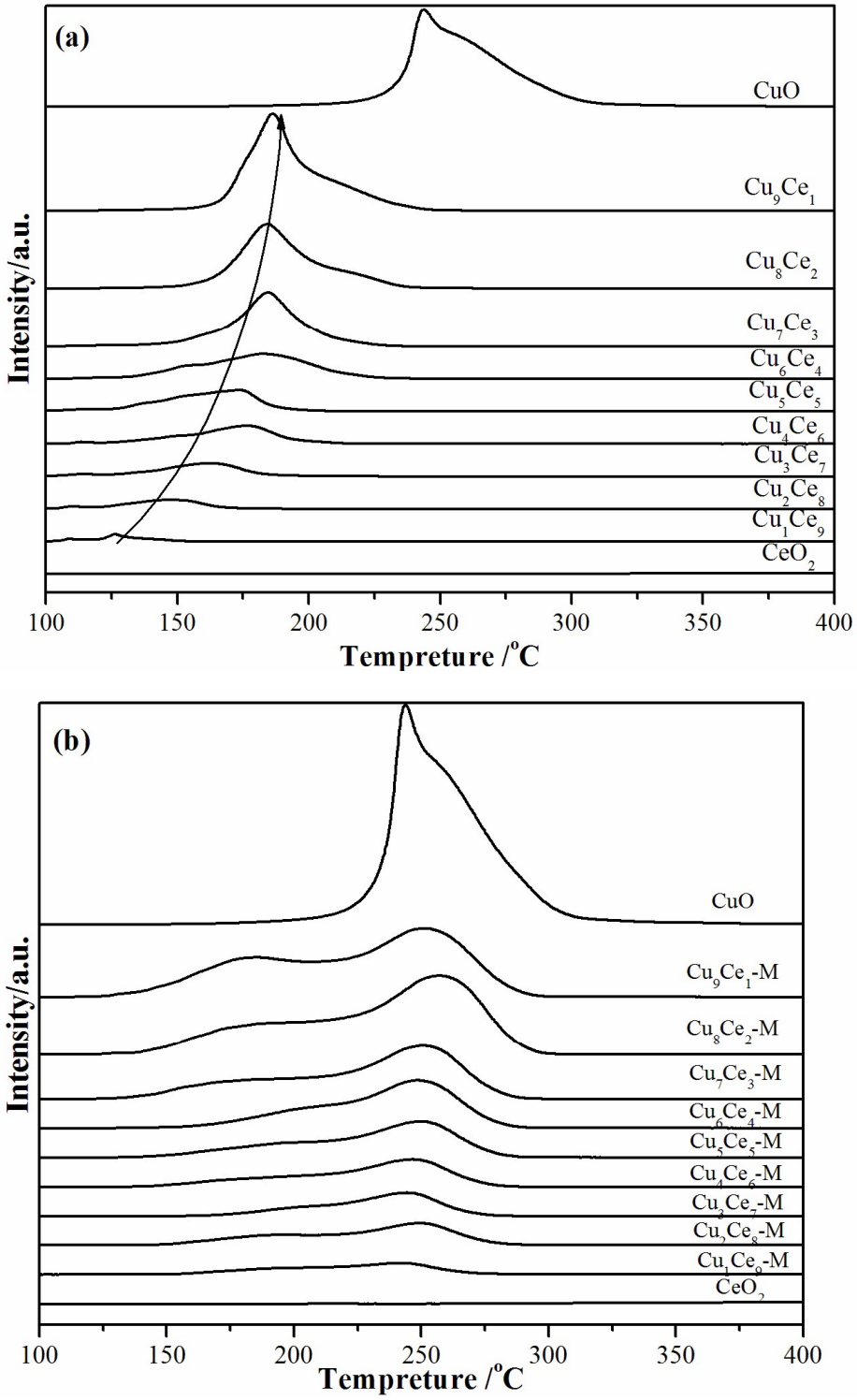

Figure 9. TPR profiles of Cu_mCe_n (a) and Cu_mCe_n-M (b) samples.

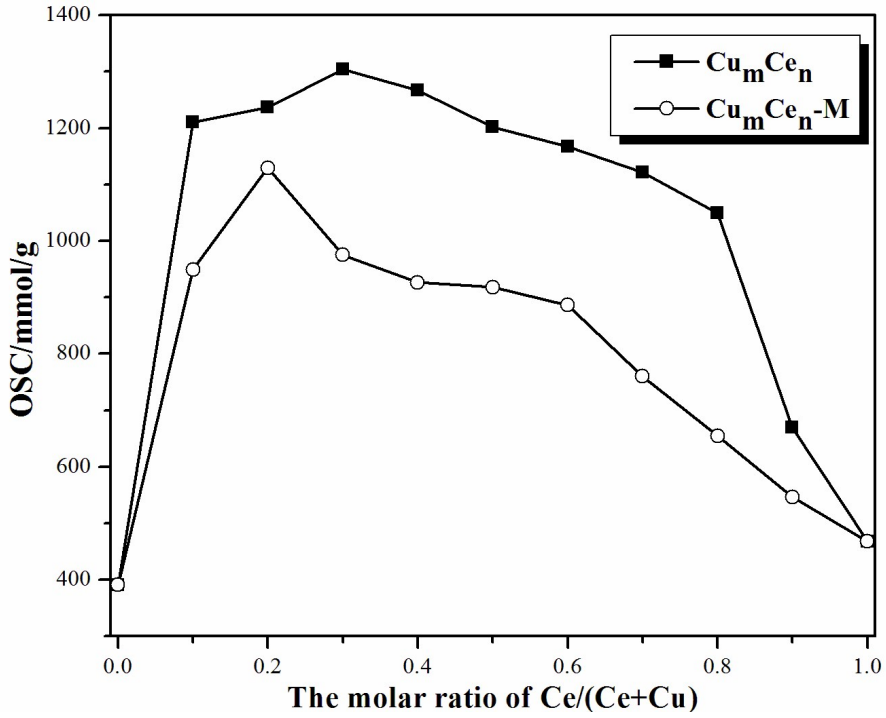

Figure 10. Oxygen storage capacity (OSC) values of the Cu_mCe_n and Cu_mCe_n-M samples.

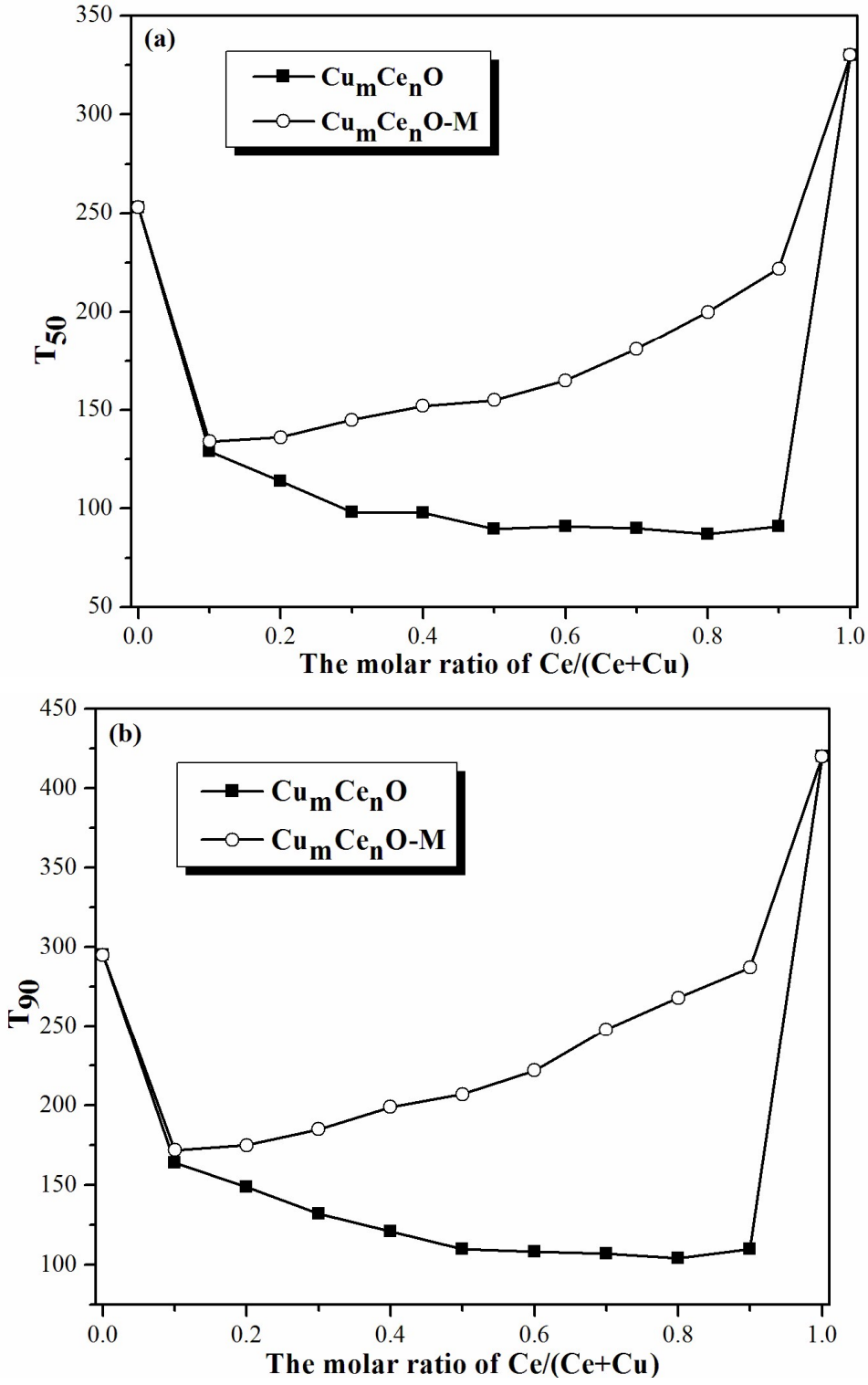

Figure 11. T_{50} (a), T_{90} (b) of the Cu_mCe_n and Cu_mCe_n-M samples.

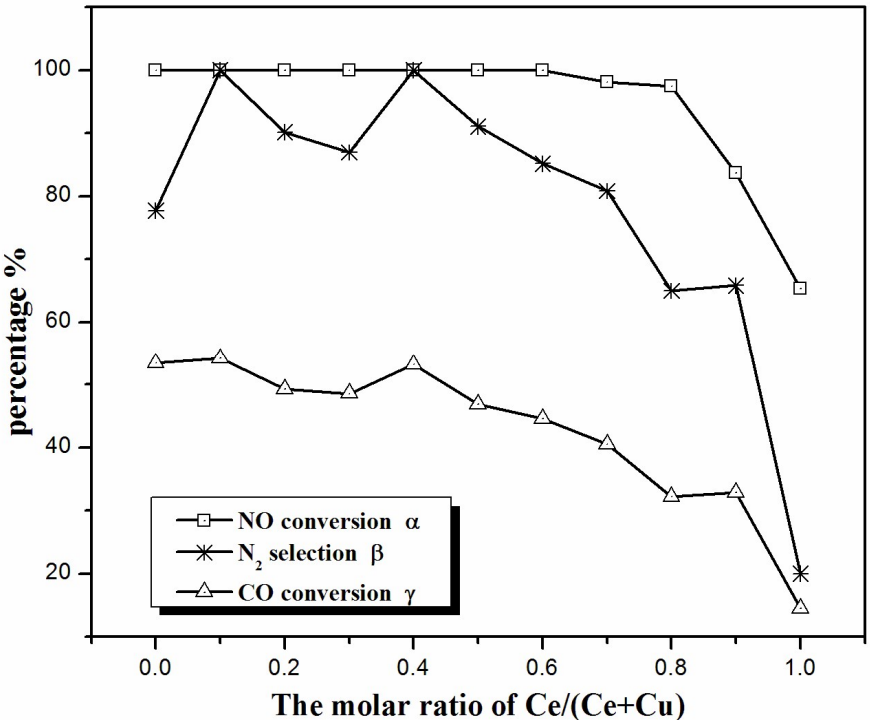

Figure 12. The experimental results of CO catalytic reduction of NO of Cu_mCe_n samples at 220 °C.

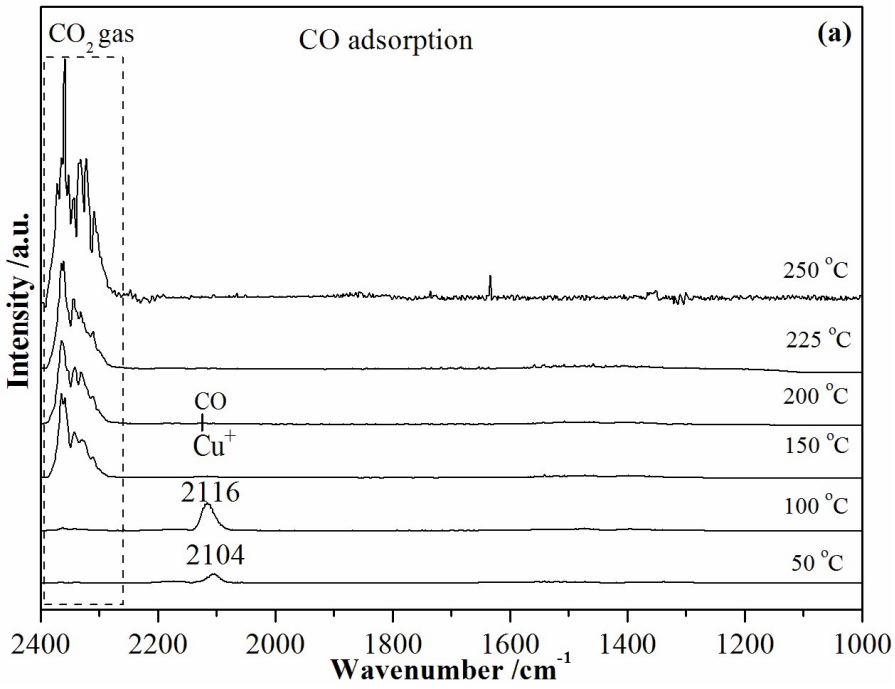

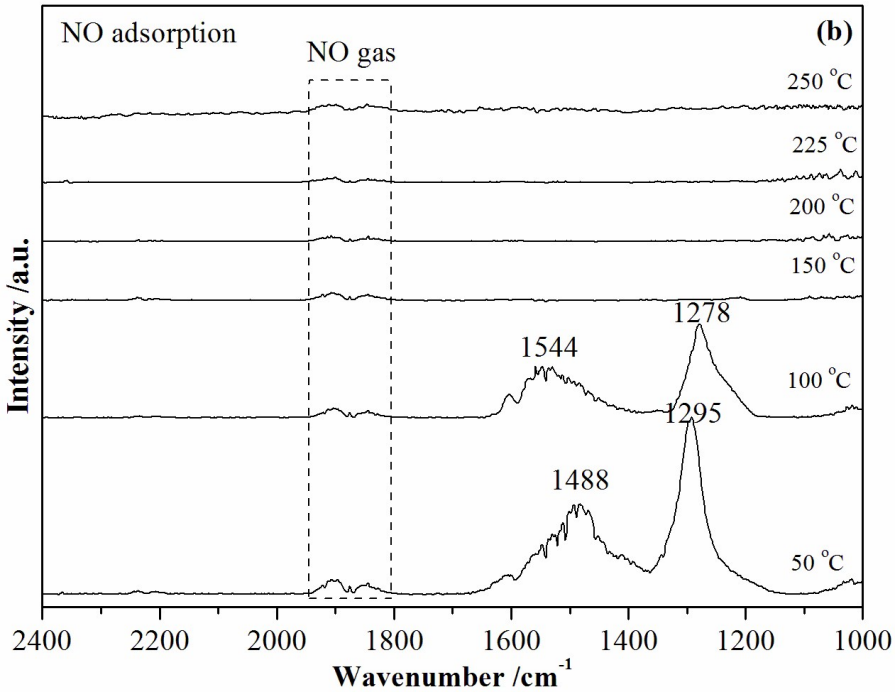

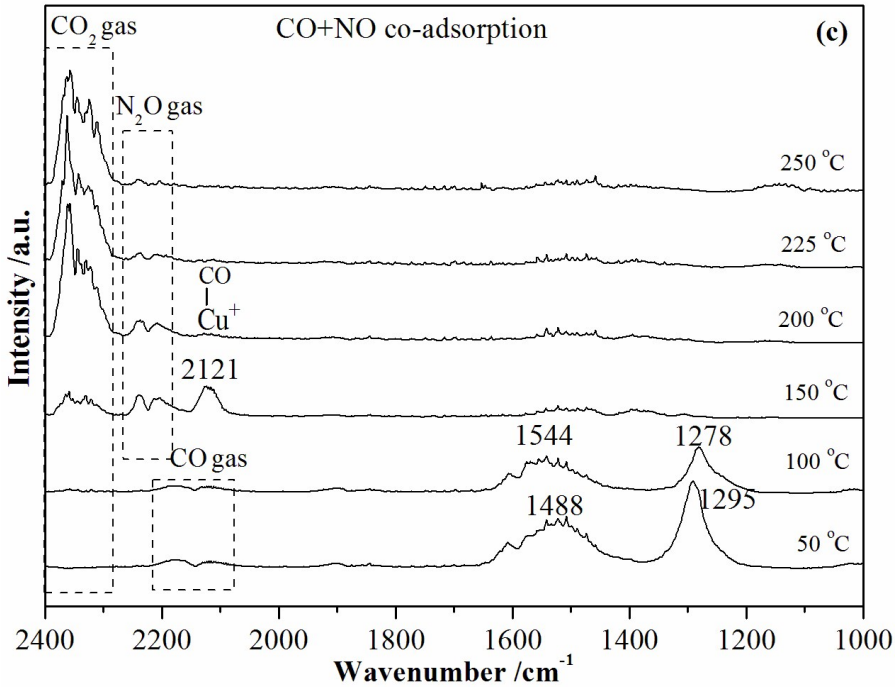

Figure 13. *In situ* DRIFTS results of CO or/and NO adsorption on the Cu9Ce1 catalyst from 50 to 250 °C.

Graphical abstract

A model of catalytic reaction mechanism of CuO-CeO_2 with two phase intergrowth and coexistence system for CO+O_2 and NO+CO.